Langmuir
Article
pubs.acs.org/Langmuir

Capacitive Monitoring of Morpholino-DNA Surface Hybridization: Experimental and Theoretical Analysis

Napoleon Tercero, Kang Wang,† and Rastislav Levicky*

Department of Chemical & Biological Engineering, Polytechnic Institute of NYU, 6 MetroTech Center, Brooklyn, New York 11201. †Current Address: School of Chemistry and Chemical Engineering, Nanjing University, Nanjing, 210093 P.R. China

Received April 11, 2010. Revised Manuscript Received June 14, 2010

Impedance and cyclic voltammetry methods, complemented by Poisson−Boltzmann (PB) modeling, are used to study hybridization of DNA analyte strands to monolayers of morpholino oligomers (MOs) immobilized by one end to mercaptopropanol-passivated gold electrodes. MOs, like peptide nucleic acids (PNAs), are uncharged molecules that recognize nucleic acids following conventional base-pairing rules. The capacitive response to hybridization, determined from real-time impedance measurements, is analyzed with emphasis on understanding the underlying structural changes and on providing a foundation for label-free diagnostics. The capacitive response is correlated with the instantaneous surface molecular populations by labeling DNA and MO strands with ferrocene tags and using cyclic voltammetry to monitor their respective coverages in real-time. This approach allows analysis of hybridization-induced changes in interfacial capacitance as a function of duplex coverage, the DC bias used for readout, buffer molarity, and probe coverage. The results indicate that unhybridized MO layers exist in a compact state on the solid support. For hybridized layers, the intrinsic signal per hybridization event is strongly enhanced at low ionic strengths but, interestingly, does not depend on the readout bias in the sampled range negative of the capacitive minimum. A PB model incorporating an effective medium description of the hybridizing films is used to establish how hybridization-derived changes in dielectric composition and charge distribution at the surface translate into experimentally observed variations in interfacial capacitance.

1. Introduction

Electrochemical detection of nucleic acid sequences continues to be widely researched[1−5] with specific techniques commanding their own dedicated reviews.[6−8] As a class of diagnostic methods, electrochemical approaches offer excellent surface specificity, low instrumentation costs, and ready integration into devices fabricated with conventional complementary-metal-oxide-semiconductor (CMOS) manufacture.[4,9−11] A distinct capability of electrochemical methods, not accessible through optical or mass based techniques, is detection of surface hybridization through the high native charge of nucleic acid analytes. Presence of this charge at an interface can be detected through various ways, such as through charge transfer (faradaic) impedance presented by hybridizing films to electroactive reporter species.[12−15] The most direct and simplest approaches, however, rely solely on alterations in the interfacial arrangement of solvent molecules, ions, and biomolecules. Such methods typically exploit field effects that alter the impedance of the underlying support on which hybridization occurs[16−19] and/or respond to changes in impedance on the solution side surrounding the hybridizing molecules.[20−22] Other reagentless methods have included transduction based on elution of hybridized molecules from the surface,[23] and on detecting conformational changes in the immobilized, "probe" capture strands.[24−26]

The effectiveness of reagentless electrochemical assays depends on selecting optimal conditions for influencing the interfacial region through hybridization. The intrinsic negative charge of DNA probes limits the range of accessible conditions, since

*To whom correspondence should be addressed. E-mail: rlevicky@poly.edu. Telephone: 718-260-3682. Fax: 718-260-3125.

(1) Drummond, T. G.; Hill, M. G.; Barton, J. K. *Nat. Biotechnol.* **2003**, *21*, 1192.
(2) Gooding, J. J. *Electroanalysis* **2002**, *14*, 1149.
(3) Wang, J. *Anal. Chim. Acta* **2002**, *469*, 63.
(4) Cagnin, S.; Caraballo, M.; Guiducci, C.; Martini, P.; Ross, M.; SantaAna, M.; Danley, D.; West, T.; Lanfranchi, G. *Sensors* **2009**, *9*, 3122.
(5) Lucarelli, F.; Tombelli, S.; Minunni, M.; Marrazza, G.; Mascini, M. *Anal. Chim. Acta* **2008**, *609*, 139.
(6) Katz, E.; Willner, I. *Electroanalysis* **2003**, *15*, 913.
(7) Daniels, J. S.; Pourmand, N. *Electroanalysis* **2007**, *19*, 1239.
(8) Fojta, M.; Jelen, F.; Havran, L.; Palecek, E. *Curr. Anal. Chem.* **2008**, *4*, 250.
(9) Ghindilis, A. L.; Smith, M. W.; Schwarzkopf, K. R.; Roth, K. M.; Peyvan, K.; Munro, S. B.; Lodes, M. J.; Stöver, A. G.; Bernards, K.; Dill, K.; McShea, A. *Biosens. Bioelectron.* **2007**, *22*, 1853.
(10) Schienle, M.; Paulus, C.; Frey, A.; Hofmann, F.; Holzapfl, B.; Schindler-Bauer, P.; Thewes, R. *IEEE J. Solid-State Circuits* **2004**, *39*, 2438.
(11) Levine, P. M.; Gong, P.; Levicky, R.; Shepard, K. L. *Biosens. Bioelectron.* **2008**, *24*, 1995.
(12) Patolsky, F.; Katz, E.; Bardea, A.; Willner, I. *Langmuir* **1999**, *15*, 3703.
(13) Pan, S.; Rothberg, L. J. *Langmuir* **2005**, *21*, 1022.
(14) Liu, J. Y.; Tian, S. J.; Nielsen, P. E.; Knoll, W. *Chem. Commun.* **2005**, 2969.
(15) Kafka, J.; Panke, O.; Abendroth, B.; Lisdat, F. *Electrochim. Acta* **2008**, *53*, 7467.
(16) Yang, W. S.; Butler, J. E.; Russell, J. N.; Hamers, R. J. *Langmuir* **2004**, *20*, 6778.
(17) Cai, W.; Peck, J. R.; van der Weide, D. W.; Hamers, R. J. *Biosens. Bioelectron.* **2004**, *19*, 1013.
(18) Fritz, J.; Cooper, E. B.; Gaudet, S.; Sorger, P. K.; Manalis, S. R. *Proc. Natl. Acad. Sci. U.S.A.* **2002**, *99*, 14142.
(19) Macanovic, A.; Marquette, C.; Polychronakos, C.; Lawrence, M. F. *Nucleic Acids Res.* **2004**, *32*, e20.
(20) Berggren, C.; Stålhandske, P.; Brundell, J.; Johansson, G. *Electroanalysis* **1999**, *11*, 156.
(21) Vagin, M. Y.; Trashin, S. A.; Karyakin, A. A.; Mascini, M. *Anal. Chem.* **2008**, *80*, 1336.
(22) Mearns, F. J.; Wong, E. L. S.; Short, K.; Hibbert, D. B.; Gooding, J. J. *Electroanalysis* **2006**, *18*, 1971.
(23) Krull, U. J.; Nikolelis, D. P.; Jantzi, S. C.; Zeng, J. *Electroanalysis* **2000**, *12*, 921.
(24) Ricci, F.; Lai, R. Y.; Heeger, A. J.; Plaxco, K. W.; Sumner, J. J. *Langmuir* **2007**, *23*, 6827.
(25) Vallee-Belisle, A.; Ricci, F.; Plaxco, K. W. *Proc. Natl. Acad. Sci. U.S.A.* **2009**, *106*, 13802.
(26) Immoos, C. E.; Lee, S. J.; Grinstaff, M. W. *ChemBioChem* **2004**, *5*, 1100.

 DOI: 10.1021/la1014384

sufficient ionic strength must be maintained to enable probe-analyte hybridization;[27] in particular, low ionic strength conditions, where electrostatic detection would be expected to be most favorable, cannot be explored. A possible solution is to utilize probes that are not charged, that is, neutral DNA analogues such as peptide nucleic acids (PNAs)[28] and morpholinos (MOs).[29] Since PNAs and MOs bind complementary DNA sequences in solution under a broad range of salt conditions,[30,31] these molecules should similarly widen the range of conditions suitable for surface hybridization. Indeed, this has first been demonstrated for PNAs by Wang and collaborators in 1996.[32]

The present report seeks to understand how ionic strength, strand coverage, and readout bias translate hybridization-induced structural changes in MO monolayers into changes in the interfacial capacitance. The research is motivated by recent efforts to develop reagentless MO-based nucleic acid assays.[33−35] While electrochemical diagnostics based on PNA probes have commanded much greater attention,[14,19,32,36−43] MOs were selected for the present study because of their synthetic and solubility advantages: whereas PNAs are limited to ~16mers, a length after which yields start to deteriorate,[44] MOs are readily prepared in the 20mer to 30mer range with little sequence restrictions. Flexibility in sequence design can be critical for applications such as pathogen detection and gene expression where longer sequences have been found to be beneficial.[45,46] MOs are also approximately 100-fold more soluble than comparable PNAs,[31] simplifying their handling in aqueous solutions during immobilization and other processing steps.

Interfacial capacitance is a direct measure of the ability of the local environment to screen electric fields and thus responds to changes in both dielectric and ionic properties. Binding of charged nucleic acid analytes to a neutral MO layer is expected to manifest through both mechanisms of contrast. To correlate the surface molecular coverages with interfacial capacitance, capacitive measurements were performed in parallel with "two-color" label-based electrochemical detection that allows quantification of both the immobilized MO "probe" and hybridized DNA "target" species. A Poisson−Boltzmann model of interfacial capacitance[35] is extended to include a structural description of the hybridizing MO films, and the model is used to explore how measured trends derive from changes in layer organization brought on by hybridization. In addition to effects from accumulation of target charge, comparison of experiment and theory identifies trends arising from thinning of the MO layer and, at sufficiently low MO coverages, its existence as a discontinuous film.

Table 1. Probe Coverages of Investigated Samples[a]

buffer strength (mol L^{-1})	LC series (cm^{-2})	IC series (cm^{-2})	HC series (cm^{-2})
0.500	1.9×10^{12}	3.5×10^{12}	6.4×10^{12}
0.100	1.4×10^{12}	3.6×10^{12}	7.5×10^{12}
0.010	1.7×10^{12}	2.8×10^{12}	7.7×10^{12}
0.001	1.3×10^{12}	3.1×10^{12}	6.7×10^{12}

[a] Determined as described in the Supporting Information, section S.3.

2. Materials and Methods

2.1. Sample Preparation. MO oligomers, of the 20mer sequence 5′ NH_2-TTT TAA ATT CTG CAA GTG AT-CO-$(CH_2)_3SS(CH_2)_3CONH_2$ 3′, were labeled with ferrocene monocarboxylic acid *N*-hydroxysuccinimide ester (FcCA-NHS) at their 5′ end. DNA oligonucleotides, of the 18mer sequence 5′ ATC ACT TGC AGA ATT TAA-$(CH_2)_3SS(CH_2)_3OH$ 3′, were labeled at their 3′ end with *N*-(2-ferrocene-ethyl) maleimide (FEM). Details of the protocols are similar to those of our earlier study[35] and are provided in the Supporting Information. MO strands were immobilized to gold working electrodes through their 3′ disulfide to serve as the "probe" in surface hybridization reactions. The DNA "target", present in solution, was complementary to the first 18 bases of the MO probes from the solution side.

Probe films were prepared on polycrystalline gold disk working electrodes, precleaned, and characterized for the roughness factor r (r = actual area/geometric area), with r ranging from 1.50 to 1.75. The working electrodes were blocked with mercaptopropanol (MCP) to suppress nonspecific contacts between the MO backbones and the gold electrode while leaving the probes attached through the 3′ thiolate.[35] The unhybridized sample structure thus consists of an underlayer of MCP and an overlayer of immobilized MO probes with their C3 linkers embedded in the MCP film. A set of 12 probe films was prepared for hybridization studies performed at four different phosphate buffer concentrations and three different ranges of probe coverage: low coverage (LC), intermediate coverage (IC), and high coverage (HC). Table 1 lists the probe coverages for all 12 samples. Further details of sample preparation are provided in the Supporting Information.

2.2. Measurements. All measurements were performed on a CHI 660C workstation (CH Instruments, Austin, TX) equipped with a three-electrode cell composed of the modified gold working electrode, a platinum wire counter electrode, and a homemade Ag/AgCl/saturated KCl reference electrode (0.197 V vs NHE at 25 °C). The reference electrode was fabricated by enclosing a 5 cm piece of 0.5 mm diameter Ag wire, coated with AgCl, in a glass sleeve (Bioanalytical Systems, West Lafayette, IN). Deposition of AgCl onto the Ag wire, after a brief etch with nitric acid, was performed at a constant current of 10 μA for 12 h under saturated KCl. All potentials are reported relative to this reference. A second glass sleeve salt bridge was used to guard against leakage of KCl from the reference electrode's reservoir into the electrolyte. The electrolyte, which also served as the hybridization buffer, consisted of various strength (0.5, 0.1, 0.01, and 0.001 mol L^{-1}) sodium phosphate buffers at pH 7.0. A fixed target concentration of 25 nmol L^{-1} was used. When data were not collected, the electrochemical cell was kept off.

Cyclic voltammetry (CV) was used to determine the instantaneous coverage of ferrocene-labeled probe and target strands,

(27) Gong, P.; Levicky, R. *Proc. Natl. Acad. Sci. U.S.A.* **2008**, *105*, 5301.
(28) Egholm, M.; Buchardt, O.; Christensen, L.; Behrens, C.; Freler, S. M.; Driver, D. A.; Berg, R. H.; Kim, S. K.; Norden, B.; Nielsen, P. E. *Nature* **1993**, *365*, 566.
(29) Summerton, J. Uncharged nucleic acid analogs for therapeutic and diagnostic applications: Oligomers assembled from ribose-derived subunits. In *Discoveries in Antisense Nucleic Acids* (*Advances in Applied Biotechnology*); Brakel, C., Ed.; Portfolio Publishing Co.: The Woodlands, TX, 1989; pp 71.
(30) Tomac, S.; Sarkar, S.; Ratilainen, T.; Wittung, P.; Nielsen, P. E.; Nordén, B.; Gräslund, A. *J. Am. Chem. Soc.* **1996**, *118*, 5544.
(31) Summerton, J. E. *Lett. Pept. Sci.* **2004**, *10*, 215.
(32) Wang, J.; Palecek, E.; Nielsen, P. E.; Rivas, G.; Cai, X.; Shiraishi, H.; Dontha, N.; Luo, D.; Farias, P. A. M. *J. Am. Chem. Soc.* **1996**, *118*, 7667.
(33) Wang, X.; Smirnov, S. *ACS Nano* **2009**, *3*, 1004.
(34) Gao, Z.; Ting, B. P. *Analyst* **2009**, *134*, 952.
(35) Tercero, N.; Wang, K.; Gong, P.; Levicky, R. *J. Am. Chem. Soc.* **2009**, *131*, 4953.
(36) Degefa, T. H.; Kwak, J. *J. Electroanal. Chem.* **2008**, *612*, 37.
(37) Aoki, H.; Buhlmann, P.; Umezawa, Y. *Electroanalysis* **2000**, *12*, 1272.
(38) Hashimoto, K.; Ishimori, Y. *Lab Chip* **2001**, *1*, 61.
(39) Kerman, K.; Ozkan, D.; Kara, P.; Erdem, A.; Meric, B.; Nielsen, P. E.; Ozsoz, M. *Electroanalysis* **2003**, *15*, 667.
(40) Uno, T.; Tabata, H.; Kawai, T. *Anal. Chem.* **2007**, *79*, 52.
(41) Aoki, H.; Tao, H. *Analyst* **2007**, *132*, 784.
(42) Keighley, S. D.; Estrela, P.; Li, P.; Migliorato, P. *Biosens. Bioelectron.* **2008**, *24*, 906.
(43) Fang, Z.; Kelley, S. O. *Anal. Chem.* **2009**, *81*, 612.
(44) Porcheddu, A.; Giacomelli, G. *Curr. Med. Chem.* **2005**, *12*, 2561.
(45) Bodrossy, L.; Sessitsch, A. *Curr. Opin. Microbiol.* **2004**, *7*, 245.
(46) Hughes, T. R.; Mao, M.; Jones, A. R.; Burchard, J.; Marton, M. J.; Shannon, K. W.; Lefkowitz, S. M.; Ziman, M.; Schelter, J. M.; Meyer, M. R.; Kobayashi, S.; Davis, C.; Dai, H.; He, Y. D.; Stephaniants, S. B.; Cavet, G.; Walker, W. L.; West, A.; Coffey, E.; Shoemaker, D. D.; Stoughton, R.; Blanchard, A. P.; Friend, S. H.; Linsley, P. S. *Nat. Biotechnol.* **2001**, *19*, 342.

S_0 and S_T (strands per area), calculated from the charge associated with oxidation/reduction of the respective tags as described in the Supporting Information. The duplex coverage S_D follows from $S_D = S_T$, and the coverage S_P of unhybridized probes from $S_P = S_0 - S_D$.

Differential surface capacitance C_d was calculated from the AC impedance (ACI) of the hybridizing electrode. In this work, ACI refers to measurements performed using a single-frequency, 5 mV rms AC potential excitation superimposed on a fixed potential bias V_{DC}. The readout frequency f depended on buffer molarity and was 8333, 2604, 368, and 32 Hz for 0.5, 0.1, 0.01, and 0.001 mol L^{-1} buffers, respectively. The frequency was chosen, for each molarity, to maintain a phase angle of 45°−50° and was determined in advance of hybridization with electrochemical impedance spectroscopy (EIS). This selection maintained a balance between resistive and capacitive impedances while avoiding distortions of the response at very high frequencies[47,48] as well as spurious interfacial charge transfer at low frequencies. Full EIS sweeps were not used for real-time tracking of hybridization because they were too slow. ACI experiments were performed under nonfaradaic conditions, so that charging currents dominated the response. For each time point along a hybridization curve, a series of ACI measurements were performed for V_{DC} settings from 0.05 to −0.20 V and back, stepped in 0.01 V increments, requiring about 40 s to complete. A hybridization run was initiated by monitoring the capacitance of the probe layer under target-free hybridization buffer every 10 min for 1 h to establish a baseline. Next, DNA target was added to 25 nmol L^{-1}, and ACI and CV measurements were performed every 5 min to track the course of hybridization.

Experimental C_d was calculated from the out-of-phase impedance Z'' according to $|Z''| = 1/(2\pi f A_g r C_d)$. This expression interprets the impedance response as that of an equivalent circuit composed of a series combination of a resistance R, representing the ohmic behavior of the buffer, and the capacitance C_d, representing charging of the interface. This model does not allow for charge transfer; that is, it assumes that, within the V_{DC} range (−0.2 to 0.05 V) of C_d measurements, only charging currents arise in response to the superimposed AC sinusoid. EIS was used to verify this assumption using MCP monolayer samples at the extremes of V_{DC}, namely, −0.2 and 0.05 V, where spurious charge transfer should be most prominent. Equivalent circuit analysis of EIS data revealed that a series combination of R and a constant phase element (CPE), where the CPE is used to represent the frequency-dependence of surface charging in EIS,[49,50] yielded the same capacitance as when an adjustable charge transfer resistance R_{CT} was in parallel with the CPE. The parallel, resistive path enables the model to short-circuit the CPE and thus account for charge transfer if the fit to experimental data requires it. The best fit R_{CT} values were of the order 10^{13}−10^{17} Ω. The result that same capacitances were obtained with or without the parallel R_{CT} path indicates that charge transfer was not an important contribution to the ACI response, that is, that the ACI measurements can be viewed as nonfaradaic.

2.3. Theoretical Calculation of C_d. Theoretical differential capacitance C_d was calculated as a function of the readout bias V_{DC} by numerically solving the Poisson−Boltzmann (PB) model described by eqs 1−4:[35]

$$C_d = \frac{d\sigma_0}{dV} \tag{1}$$

$$\sigma_0 = -\varepsilon\varepsilon_0 \left(\frac{dV}{dx}\right)_{0+ \leftarrow x} \tag{2}$$

$$\frac{d^2V}{dx^2} = -\frac{\rho(x)}{\varepsilon(x)\,\varepsilon_0} \tag{3}$$

$$\rho(x) = -ec_{im}(x) + \sum_j z_j e c_{j,B} \exp(-z_j eV(x)/kT) \exp(-\beta_j(x)) \tag{4}$$

where σ_0 is the charge per area on the electrode, x is the normal distance from the electrode into the sample, $\varepsilon(x)$ is the dielectric constant, ε_0 is the permittivity of free space, $\rho(x)$ is the charge concentration, c_{im} is the number concentration of immobilized charges (i.e., from bound DNA targets), T is the absolute temperature, k is the Boltzmann constant, and z_j, $c_{j,B}$, and β_j are the signed valence, solution number concentration, and partitioning penalty of species j, respectively. The partitioning penalty $\beta_j(x)$ is in units of kT; the penalty for species j to partition from solution to a distance x from the electrode is therefore $\beta_j(x)kT$. The buffer environment was assumed to possess a dielectric constant of 80 and ionic composition of Na^+, $H_2PO_4^-$, HPO_4^{2-}, and PO_4^{3-} as calculated using pK_a values of 2.15, 6.87, and 12.3 and experimental total phosphate molar concentration C_B, at a pH of 7.0. The number concentration c_B follows from $c_B = N_A C_B$, where N_A is Avogadro's number. A full description of the solution methodology can be found in ref 35. In experiments, the potential perturbation dV in eq 1 is provided by the 5 mV AC modulation. Similar approaches have been previously used to simulate field-effect semiconductor biosensor devices.[51,52]

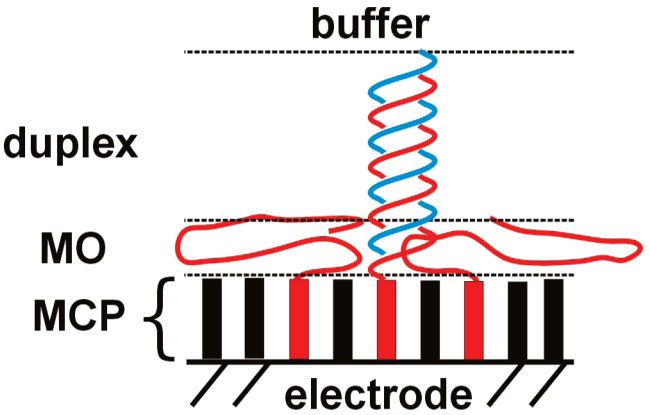

Figure 1. Description of sample structure used for PB modeling.

The central challenge in the calculation of C_d is to connect the PB formalism of eqs 1−4 to a structural description of the sample that accounts for dominant changes arising from hybridization. The sample structure was described as consisting of an MCP layer, a layer of unhybridized MO probes, and a layer of MO−DNA duplexes that protrudes above the MO layer (Figure 1). Based on results to be presented in section 3, unhybridized MO probes were assumed to exist in a collapsed state on the solid support, rather than dangle into solution. For simplicity, the

(47) Huang, V. M.-W.; Vivier, V.; Orazem, M. E.; Perbere, N.; Tribollet, B. *J. Electrochem. Soc.* **2007**, *154*, C81.
(48) Orazem, M. E.; Tribollet, B. *Electrochemical Impedance Spectroscopy*, 3rd ed.; Wiley & Sons, Inc.: Hoboken, NJ, 2008.
(49) For modeling EIS data, a constant phase element (CPE), instead of an ideal capacitor, was used to better account for the impact of interfacial heterogeneities on charging response that becomes apparent in frequency-sweep measurements. The CPE ideality exponent n was between 0.96 and 0.97, where $n = 1$ corresponds to an ideal capacitor. This indicates a fairly low degree of heterogeneity (e.g., see Douglass, E. F., Jr.; Driscoll, P. F.; Liu, D.; Burnham, N. A.; Lambert, C. R.; McGimpsey, W. G. *Anal. Chem.* **2008**, *80*, 7670).
(50) Brug, G. J.; van den Eeden, A. L. G.; Sluyters-Rehbach, M.; Sluyters, J. H. *J. Electroanal. Chem.* **1984**, *176*, 275.
(51) Landheer, D.; Aers, G.; McKinnon, W. R.; Deen, M. J.; Ranuarez, J. C. *J. Appl. Phys.* **2005**, *98*, 044701.
(52) McKinnon, W. R.; Landheer, D.; Aers, G. *J. Appl. Phys.* **2009**, *104*, 124701.

DOI: 10.1021/la1014384 C

Table 2. Parameters Used in PB Modeling

layer	ε	t (nm)	β_{Na^+}	$\beta_{H_2PO_4^-}$	$\beta_{HPO_4^{2-}}$	$\beta_{PO_4^{3-}}$	c_{im}
MCP	4.4	0.67	1000	1000	1000	1000	0
MO	9.1	eq *5*	0	1.8	1000	1000	eq *6*
MO−DNA duplex	eq *7*	$3r_D$	0	0	0	0	eq *6*

thickness of the duplex layer was taken to equal the length of an MO−DNA hybrid. Within each of the layers ε, c_{im}, and β_j were assumed to be uniform. Table 2 summarizes the corresponding parameter values.

Table 2, row 1 shows that the MCP layer was treated as an ion-impermeable (i.e., high β_j) dielectric with a permittivity of 4.4 and a thickness of 0.67 nm. This permittivity is consistent with those reported in the literature for −OH terminated SAMs,[35,53] and the thickness was calculated from $t_{MCP} = \sigma m/(dN_A)$, where the mass density of MCP is $d = 1.07$ g cm^{-3}, the surface coverage σ is taken to be 4.7×10^{14} molecules cm^{-2},[54] and the molar mass $m = 92$ g mol^{-1}.

The second row in Table 2 represents the layer of collapsed MO probes. The ε value of 9.1, as well as all four β values, were taken from Tercero et al.[35] where they were found to satisfactorily describe a probe layer at a coverage of 4.9×10^{12} cm^{-2}. The thickness of a collapsed layer of MO *N*mers is obtained from

$$t_{MO} = v_{RES} N S_P/(1-\theta) \quad (5)$$

where the volume of an MO residue v_{RES} was assumed to equal that of a DNA nucleotide, or 0.53 nm^3, and the number N of residues per probe equals 20. The fractional surface coverage of duplexes θ follows from $\theta = a_D S_D$, where a_D is the duplex cross section which was taken to be same as that for DNA; thus, $a_D = \pi$ nm^2. Assuming perpendicularly oriented duplexes, $1-\theta$ is the fraction of surface left to the unhybridized probes. The concentration of immobilized charge c_{im}, originating from hybridized DNA targets, is given by

$$c_{im} = |z_D| S_D / l_D \quad (6)$$

where $|z_D| = 11$ is the number of charges in an MO−DNA duplex. This charge arises from the 18mer targets and is corrected for an expected 40% reduction due to counterion condensation.[55] $l_D = 6.1$ nm is the duplex length, taking 0.34 nm as the rise per base pair.

The MO−DNA duplex layer is described by the third row of Table 2. Since this layer represents a mixture of duplexes and buffer, the dielectric constant ε_L was calculated according to the Bruggeman effective medium expression for a two component mixture[56,57]

$$\phi_1 \frac{\varepsilon_1 - \varepsilon_L}{\varepsilon_1 + 2\varepsilon_L} + (1-\phi_1)\frac{\varepsilon_2 - \varepsilon_L}{\varepsilon_2 + 2\varepsilon_L} = 0 \quad (7)$$

where ε_1 and ε_2 are the pure state permittivities of the two components, present in the mixture at volume fractions ϕ_1 and $\phi_2 = 1 - \phi_1$, respectively. The volume fraction for duplexes, if the duplexes are assumed to orient normally to the solid support, follows from $\phi_1 = \theta = a_D S_D$. Without availability of ε for MO−DNA duplexes, ε_1 is simply assumed to be the same as that for unhybridized MO strands, $\varepsilon_1 = 9.1$. This is likely an over-simplification insofar as ε_1 would also carry contributions from water of hydration, which may be expected to significantly differ for MO and MO−DNA. The buffer dielectric constant is set to $\varepsilon_2 = 80$. Since the duplex layer is expected to be well solvated and permeable to all ions, β_j are taken to be 0 for all j. For purposes of calculation, the thickness of the duplex layer was limited to three Debye lengths r_D[58] because numerical integration, especially at higher ionic strengths, was challenged by rapid decay of the electric field within the layer. Comparison to calculations truncated after $5r_D$ confirmed that the impact on the derived C_d was minimal (difference in $C_d \sim 0.01\%$).

The Debye lengths for modeled conditions range from 0.30 to 2.1 nm, corresponding to buffer molarities from 0.5 to 0.01 mol L^{-1}. Since electrochemically polished electrodes are expected to have much of the roughness at lengths scales below 10 nm removed,[59] surface roughness should be dominated by features greater than the Debye length; therefore, the double layer should be largely conformal to the contour of the surface. These considerations are consistent with a sample description for which the interfacial roughness does not appear as a smeared interface.

With the inputs as summarized in Table 2, the PB model is fully specified and its predictions can be compared to experimental trends. Before doing so, however, it is useful to recognize its key simplifications. By assuming that hybridized MO−DNA duplexes always exist in a perpendicular orientation to the solid support, the model neglects possible dependence of the orientation on readout potential,[60,61] ionic strength, and duplex−duplex interactions. This assumption is partially justified through use of readout potentials that fall negative of the capacitive minimum (section 3), and which therefore correspond to negatively charged surfaces that are repulsive to duplexes and should favor an orientation toward the normal.

Treatment of large ions, such as phosphate, as point charges when their dimensions are nearly comparable to the width of a collapsed MO layer is also a strong simplification. This assumption may be reflected in the high values for the βs of multivalent phosphate species HPO_4^{2-} and PO_4^{3-} in the MO layer ($\beta = 1000$, Table 2). These β settings are motivated by the result that if HPO_4^{2-} is allowed to partition into the MO layer then a much sharper upturn in calculated C_d with positive V_{DC} is derived, due to the strong attraction for the divalent phosphate, than observed in experiment. Physically, the need to exclude these ions may originate from geometric constraints due to their size or, as previously speculated,[35] from difficulty of supporting multiply ionized phosphate states in the low ε environment of the MO film. The model moreover neglects dielectric and thickness changes in the MO layer that would be expected to result from ion entry, as well as dependence of the solvent dielectric constant on ionic concentrations. These assumptions avoid the introduction of difficult to estimate parameters into the model. For similar reasons, the partitioning penalties were assumed not to vary with strand coverage, though such dependence is expected and would require a detailed study in its own right.

Last, the theory assumes that the probe and duplex layers are uniform in composition, normal to the solid support as well as laterally. In this hypothetical situation, C_d is uniform over the surface. In experiments, however, this will not apply in general. For example, for a duplex layer at coverage of $\sim 1 \times 10^{11}$ cm^{-2} typical of the LC series, the average separation between duplexes is about 30 nm, compared with just a ~5 nm molecular size. Thus, significant lateral variations in composition, potential, and local C_d should be present that are not addressed by the one-dimensional PB model, though a theory aiming to quantitatively explain experimental behavior would need

(53) Sondag-Huethorst, J. A. M.; Fokkink, L. G. J. *Langmuir* **1995**, *11*, 2237.
(54) Strong, L.; Whitesides, G. M. *Langmuir* **1988**, *4*, 546.
(55) Record, M. T.; Anderson, C. F.; Lohman, T. M. *Q. Rev. Biophys.* **1978**, *11*, 103.
(56) Bruggeman, D. A. G. *Ann Phys.* (*Leipzig*) **1935**, *416*, 636.
(57) Landauer, R. *J. Appl. Phys.* **1952**, *23*, 779.

(58) $r_D = (\varepsilon\varepsilon_0 kT/2N_A e^2 I_S)^{1/2}$, where $I_S = 1/2(\Sigma_i z_i^2 C_{i,B})$, $\varepsilon = 80$ is the relative permittivity of water, ε_0 is the permittivity of vacuum, and k is the Boltzmann constant.
(59) Douglass, E. F., Jr.; Driscoll, P. F.; Liu, D.; Burnham, N. A.; Lambert, C. R.; McGimpsey, W. G. *Anal. Chem.* **2008**, *80*, 7670.
(60) Kelley, S. O.; Barton, J. K.; Jackson, N. M.; McPherson, L. D.; Potter, A. B.; Spain, E. M.; Allen, M. J.; Hill, M. G. *Langmuir* **1998**, *14*, 6781.
(61) Rant, U.; Arinaga, K.; Fujita, S.; Yokoyama, N.; Abstreiter, G.; Tornow, M. *Nano Lett.* **2004**, *4*, 2441.

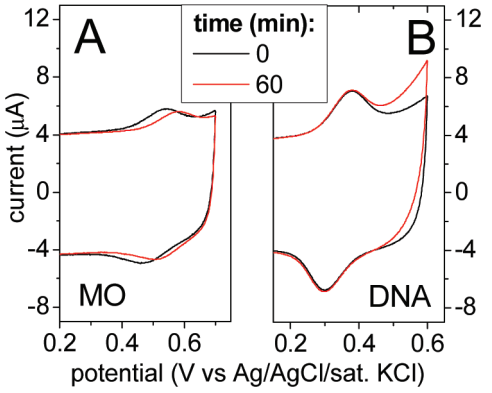

Figure 2. (A) Time evolution, over the course of 60 min, of cyclic voltammograms for a low coverage (LC series; $S_0 = 1.7 \times 10^{12}$ cm^{-2}) unhybridized MO layer, under 0.01 mol L^{-1} sodium phosphate, pH 7. (B) As in (A) but for an unhybridized DNA probe layer ($S_0 = 3.4 \times 10^{12}$ cm^{-2}). Other settings: scan rate 20 V s^{-1}.

to account for such heterogeneity. Because of this and the other assumptions inherent to the PB model, its quantitative fitting to experimental data is not expected to be very meaningful; rather, model parameters were fixed or calculated as in Table 2, and the model was restricted to providing general insight into how molecular organization of the interface qualitatively translates to experimental C_d trends.

3. Results and Discussion

Understanding the capacitive response to hybridization rests in part on a correct picture of the initial, unhybridized state of the layer. This initial state is believed to consist of aggregated, desolvated probes, for several reasons. First, organization of unhybridized MO films is subject to their moderate solubility, which falls in the mmol L^{-1} range. Since the MO concentration inside a probe layer will exceed this solubility limit, unhybridized MO probes exist under conditions when they are expected to precipitate. Second, an initial analysis of the charging response of MO layers was consistent with a collapsed, desolvated state.[35] Third, such an organization is also supported by the redox behavior of unhybridized MO probes (Figure 2).

Figure 2 compares the time-dependence of CV traces of an FcCA-labeled MO film (Figure 2A) with that of the same sequence, FcCA-labeled DNA probe layer (Figure 2B). For the MO film, from $t = 0$ min when the layer was first transferred to hybridization buffer to $t = 60$ min, there was a 0.04 V positive shift in the FcCA formal potential to $E° = 0.55$ V. Most of this change occurred within the first 30 min, with little additional shift discerned thereafter. The displacement in $E°$ was observed at all MO probe coverages that were studied.[62] In contrast, no such change in redox behavior was observed with DNA probes (Figure 2B). A positive displacement of the redox potential indicates that the ferrocene tags became more difficult to oxidize when attached to MO probes, when the layers were allowed to age.[63] Therefore, use of MO probes leads to stabilization, with time, of the neutral ferrocene relative to its oxidized ferricinium state. We propose these observations are explained by aggregation of the MO probes in which the FcCA tags, which are likewise hydrophobic, associate with the desolvated aggregates and

(62) Higher coverages increased $E°$, such that $E° = 0.57$ V for the HC series samples.

(63) Since the displacement is not accompanied by an opposite movement of the anodic and cathodic peaks along the potential axis, it is not attributed to electron transfer limitations or to uncompensated resistance.

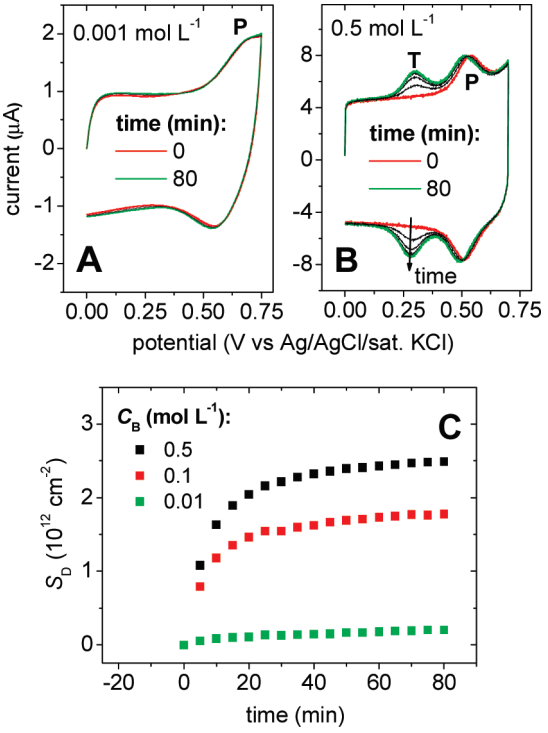

Figure 3. Cyclic voltammetry traces showing progress of hybridization for IC series under (A) 0.001 mol L^{-1} and (B) 0.5 mol L^{-1} phosphate buffer, pH 7. "T" indicates the FEM target peak; "P" stands for the probe FcCA peak. In both (A) and (B), initial ($t = 0$) and final ($t = 80$ min) curves are shown in red and green, respectively. Intermediate times at 5, 15, 35, 55, and 65 min are shown in black. These curves are not distinguishable in (A) because no hybridization was observed, while the last several traces in (B) overlap as hybridization reached steady state. (C) CV-derived time traces of duplex coverage S_D for the IC coverage series at three buffer concentrations.

become less exposed to the solvent environment. Association of the tags with MO aggregates would hinder their oxidation, with a concomitant positive shift in $E°$, because it interferes with stabilization of the charged ferricinium state by interactions with water and solution ions. In comparison, the more soluble DNA probes cannot sequester tags in this fashion so that no shift in $E°$ is observed.

Figure 3A and B illustrates CV tracking of hybridization for the IC series under two ionic strengths. The time $t = 0$ corresponds to addition of the fully complementary target to a concentration of 25 nmol L^{-1}. In the 0.5 mol L^{-1} buffer, addition of targets is immediately followed by appearance of signal from their FEM tags ("T" peak in Figure 3B). In 0.001 mol L^{-1} buffer, hybridization could not be detected for any of the coverage series and, in addition, no hybridization was observed for the HC series in 0.01 mol L^{-1} buffer. Figure 3C shows sample time traces of the duplex coverage S_D obtained from conversion of the T peak charge to strand coverage, following the method described in section S.3 of the Supporting Information.

Each CV scan was preceded by an ACI measurement of the differential capacitance C_d at V_{DC} settings from 0.05 to −0.2 V. Examples of C_d time traces are shown in Figure 4A. Exposure to noncomplementary sequences did not produce significant responses either in capacitive or CV modes (Supporting Information, section S.4). Interestingly, for a given hybridization run, curves measured at V_{DC} settings between −0.2 and +0.05 V could be superimposed by translation along the C_d axis. This curious independence of the hybridization signal on readout bias was

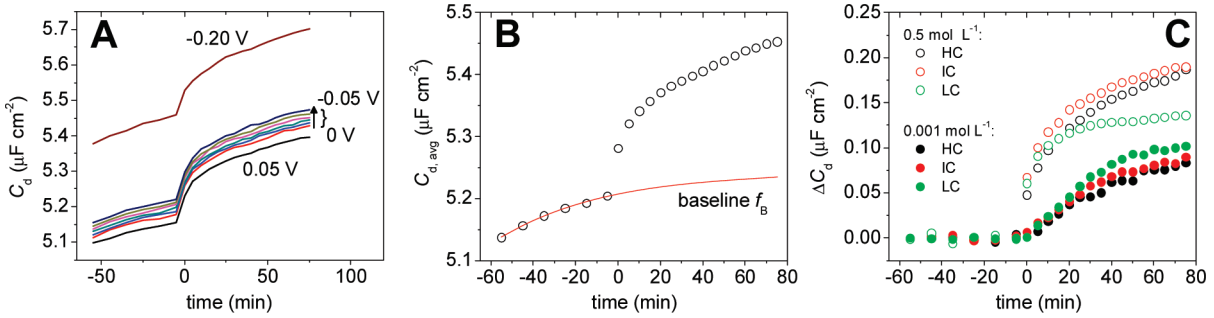

Figure 4. Processing of capacitance data. (A) Hybridization tracking through changes in interfacial capacitance for the IC series in 0.5 mol L^{-1} phosphate buffer. $t = 0$ marks introduction of target DNA to a concentration of 25 nmol L^{-1}. The various $C_d(t)$ curves were taken on the same sample but at different DC biases, ranging from 0.05 down to −0.2 V. (B) The six $C_d(t)$ curves from 0 to −0.05 V in (A) were averaged, producing the $C_{d,avg}$ curve. The six points prior to addition of target are used to estimate the baseline correction f_B described in the text. (C) Final $\Delta C_d = C_{d,avg} - f_B$ curves for all three coverage series, at the highest and lowest buffer concentrations.

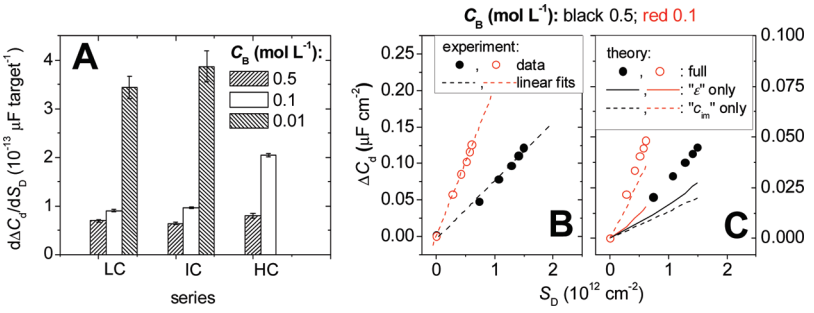

Figure 5. (A) Sensitivity factor $d\Delta C_d/dS_D$, obtained from initial ($t \leq 25$ min) slopes of ΔC_d versus S_D curves, for all conditions for which S_D could be independently confirmed through CV measurements. Error bars are standard deviation of the linear fits. (B) $\Delta C_d(S_D)$ data for HC series in 0.5 mol L^{-1} (black points) and 0.1 mol L^{-1} (red points) buffer concentrations. Dashed lines are linear fits from which $d\Delta C_d/dS_D$ values were derived. (C) Predictions from PB calculations for the data in (B) accounting for both dielectric ("ε") and immobilized charge ("c_{im}") contributions (points), dielectric contributions only (solid lines), or contributions from immobilized charge only (dashed lines). Black traces, 0.5 mol L^{-1} conditions; red traces, 0.1 mol L^{-1} conditions.

confirmed for all examined combinations of S_0 and C_B. The independence does not hold in general; indeed, at more positive biases, an inversion in contrast where C_d decreases rather than increases with hybridization is possible.[35] Although the physical origins of the independence are not understood, the available evidence suggests it is only observed for V_{DC} values negative of the potential of zero charge (pzc). The pzc can be determined for unhybridized MO films from the minimum in the C_d versus V_{DC} curve;[64] all of the conditions of this study fall negative of the pzc. From a pragmatic perspective, since V_{DC} does not impact sensitivity, the readout bias should be selected based on other considerations, for example, choice of gentle biases that minimize degradation of probe films and improve signal stability. In the present study, as discussed below, the effect was exploited to perform data averaging to provide a more accurate baseline correction.

C_d measurements exhibited "drift" attributed to loss of MCP molecules (section S.5, Supporting Information) that leads to an increase in C_d with time even in the absence of hybridization. The resultant time-dependent baseline was mathematically handled as illustrated in Figure 4B by assuming it follows the monoexponential decay $f_B = A_1 - A_2\, e^{-kt}$ where A_1, A_2, and k are derived from a fit to the prehybridization ($t < 0$) history of a sample. A physically motivated derivation of f_B is provided in section S.6 of the Supporting Information. An example of such a fit is plotted as the red trace in Figure 4B, from which the change in capacitance due to hybridization, ΔC_d, is obtained using $\Delta C_d = C_d - f_B$. Figure 4C shows the resultant ΔC_d curves for all three coverage series at the highest (0.5 mol L^{-1}) and lowest (0.001 mol L^{-1}) buffer concentrations. These results show that capacitive transduction was able to cleanly resolve hybridization even under 0.001 mol L^{-1} buffer, for which CV analysis failed (cf. Figure 3A).

From the results in Figure 4C, it follows that DNA analyte at 25 nmol L^{-1} was detected with higher sensitivity in the more concentrated, 0.5 mol L^{-1} buffer. However, this sensitivity derives from a greater overall extent of hybridization (i.e., more bound targets per area), enabled by weakened electrostatic repulsions between bound targets under the higher ionic strength. Although often sensitivities are quoted in this manner, based on detectable concentration of analyte, it is important to recognize that such metrics depend on thermodynamics of binding. Thus, very low analyte concentrations can be detected if the binding affinity is high (i.e., sufficiently long sequences are used) and if a large number of analyte molecules is available to drive up the surface-bound yield. Such measurements, therefore, do not report directly on the ability of an assay to translate a single binding event into a detectable signal.

A more informative measure of sensitivity would be the response per binding event. The argument also can be made that the response per binding event is the more useful metric in many situations, since the target is often the limiting reagent, for example, in gene expression assays where transcript concentrations can be ~1 pmol L^{-1}.[65] In such situations, the response per binding event can directly predict the maximum possible signal realizable in the limit that all targets are bound. In our case,

(64) Bard, A. J.; Faulkner, L. R. *Electrochemical Methods: Fundamentals and Applications*, 2nd ed.; Wiley & Sons, Inc.: New York, 2000.

(65) Chudin, E.; Walker, R.; Kosaka, A.; Wu, S. X.; Rabert, D.; Chang, T. K.; Kreder, D. E. *Genome Biology* **2002**, *3*, research0005.1.

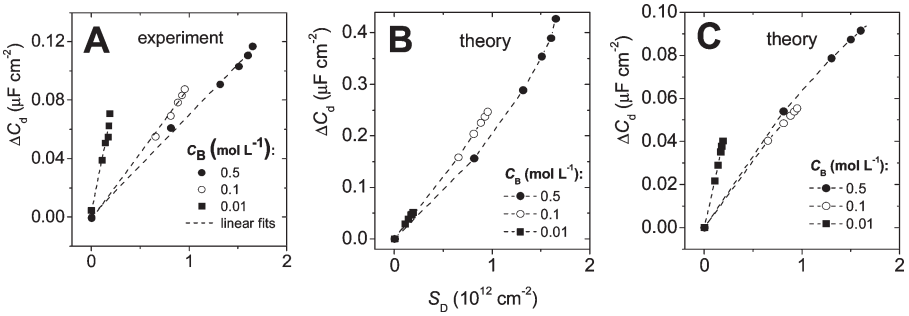

Figure 6. (A) Experimental and (B,C) predicted $\Delta C_d(S_D)$ curves for LC series samples. In (B), the MO layer was assumed to be of decreasing thickness but to remain continuous as it hybridizes, whereas in (C) it is taken to remain of fixed thickness while becoming increasingly discontinuous.

the "per duplex" sensitivity can be quantified by the parameter $d\Delta C_d/dS_D$, representing the increment $d\Delta C_d$ in signal per increment dS_D in duplex coverage. Using ΔC_d and S_D determined from the parallel ACI and CV analyses, $d\Delta C_d/dS_D$ values were derived from linear fits to experimental ΔC_d versus S_D plots for $t \leq 25$ min. Data for higher t were not included because the baseline extrapolation, especially for low MO probe coverages, was observed to lose accuracy at longer times. Figure 5A shows a prominent increase in sensitivity per hybridization event as buffer molarity decreases, a trend that holds for all three coverage series. In addition, $d\Delta C_d/dS_D$ increased from the IC to the HC series, suggesting improved sensitivity as probe coverage increased. Figure 5B shows fitted data (points) and linear fits (dashed lines) for the HC series, while Figure 6A shows fitted data and fits for the LC series.

The PB model of section 2.3 was used to simulate expected capacitive responses for various scenarios in order to explore physical origins of the observed trends. For the calculations, V_{DC} was chosen to be at comparable negative offset (−0.1 to −0.2 V) relative to the minimum in the capacitance versus potential curve for unhybridized films ($S_D = 0$) as used in analysis of experimental data. C_d was calculated using experimental values of S_D, C_B, S_0, and $S_P = S_0 - S_D$, with additional inputs as described in section 2.3 and Table 2. ΔC_d was obtained by subtracting the value of C_d calculated for $S_D = 0$, $\Delta C_d = C_d(S_D) - C_d(0)$. The model was used to separately consider contributions to ΔC_d from (1) dielectric "ε" changes that arise from thinning of the MO layer as probes are consumed to become duplexes and from accompanying permittivity changes in the duplex layer as the duplex volume fraction increases, and (2) immobilized charge "c_{im}" contributions from accumulation of negative target charge. c_{im} influences the interfacial capacitance by altering the local concentrations of mobile ions, since it attracts cations and repels anions. The relative importance of these two contributions can be compared through "full" calculations that include both the "ε" and "c_{im}" effects, the dielectric "ε" effects only (i.e., enforcing $c_{im} = 0$), or only the "c_{im}" contribution while keeping layer thicknesses and permittivities unchanged.

Figure 5C compares theoretical curves for the "full" (points), "ε only" (solid curves), and "c_{im} only" (dashed curves) scenarios for the HC series. Good agreement is observed in qualitative trends between experiment and the "full" scenario expected to be most representative of reality. In terms of magnitude, the calculated ΔC_d is lower by about 60% than that measured. Given the approximations inherent to the PB model (section 2.3) and uncertainties in input parameters, this agreement within a factor of 2 to 3 appears reasonable.

The calculations of Figure 5C point to several additional conclusions. First, in the more concentrated 0.5 mol L^{-1} buffer, "ε" effects (solid line) dominate slightly over those due to "c_{im}" (dashed line), but the influence of "c_{im}" becomes dominant as buffer concentration decreases to 0.1 mol L^{-1}. This suggests the improvement in diagnostic sensitivity at low buffer molarities (Figure 5A) is attributed to accumulation of target charge rather than to dielectric changes. Second, by comparing calculations for the various scenarios, the slight positive curvature in the theoretical "full" response for 0.5 mol L^{-1} can be attributed to dielectric effects and in particular to thinning of the probe layer. It is reasonable to suppose that the slight curvature in the corresponding experimental data at 0.5 mol L^{-1} (Figure 5B) may also reflect this effect. Third, by comparing the "ε only" traces for the 0.5 and 0.1 mol L^{-1} conditions, even these purely dielectric changes are seen to depend on buffer molarity. This reflects dependence of C_d on the local concentrations of mobile ions, which are governed by the corresponding solution concentrations as well as the layer thicknesses and permittivities that determine the surface potential profile.

Figure 6 compares experimental data (Figure 6A) with PB predictions (Figure 6B and C) for the LC series data. In Figure 6B, the MO probe layer was assumed to remain continuous, with hybridization accommodated through layer thinning as for the HC data discussed above. By comparing Figure 6B and A, it is evident that this scenario does not correctly capture the data as it fails to account for the increase in sensitivity at 0.01 mol L^{-1} relative to the higher concentrations. Since the assumption of continuity is questionable at these low coverages, alternately the MO layer can be viewed as remaining at a *constant* thickness but with an adjustable volume fraction of solvent-filled voids. In this case, hybridization leads to an increase in the void fraction as probes become transferred to the duplex layer, causing the layer permittivity to vary. The variation in permittivity can be obtained from the effective medium eq 7, with the nonsolvent volume fraction calculated according to $\phi_1 = S_P/S_P^* + a_D S_D$, where S_P^* is the minimal coverage required for a continuous layer of unhybridized probes. The S_P/S_P^* term ($S_P < S_P^*$) represents the volume fraction of unhybridized probes in the MO layer, while the $a_D S_D$ term accounts for contributions from the normal-oriented duplexes; together, these two contributions represent the nonsolvent fractional volume.

Representation of the MO layer as of fixed thickness but with an adjustable void fraction leads to significantly improved agreement with experiment, as shown in Figure 6C for $S_P^* = 5 \times 10^{12}$ cm^{-2}. This result strongly argues that the MO film must be interpreted as discontinuous at these low coverages. In addition to qualitatively capturing the enhancement in sensitivity in 0.01 mol L^{-1} buffer, the calculations also reproduce the similarity in sensitivities observed for the 0.1 and 0.5 mol L^{-1} samples. The similar response for the latter two samples reflects compensation between

dielectric effects, which are stronger for the 0.5 mol L^{-1} specimen due to its higher probe coverage (Table 1) and hence starting ε_L further away from that of the solvent (i.e., higher initial dielectric contrast), and "c_{im}" contributions which are stronger for the 0.1 mol L^{-1} sample due to decreased ionic strength.

The dielectric effects can be tuned by adjusting S_P*; for example, for S_P* of 6×10^{12} cm^{-2}, the 0.1 mol L^{-1} curve in Figure 6C would lie above the 0.5 mol L^{-1} curve, just as seen in experiment. S_P* of 6×10^{12} cm^{-2}, on the other hand, would lead to somewhat worsened agreement for the 0.5 mol L^{-1} HC data in Figure 5C, since it predicts a sudden transition to discontinuous behavior as hybridization proceeds and the coverage of unhybridized probes drops below that required for continuity. A more refined structural description of layer thinning leading to its breakup (e.g., with both effects contributing at intermediate coverages) might be able to better account for evolution of the MO organization. As previously seen for the HC data, again the theory underpredicts the measured response, in this case by about 30−40%.

4. Conclusions

Unhybridized layers of 20mer morpholinos (MOs), end-tethered to mercaptopropanol passivated gold working electrodes, gradually rearrange their organization. The reorganization is consistent with formation of desolvated MO aggregates on the solid support. Nevertheless, MO probes remain active toward hybridization with DNA analyte. Differential capacitance (C_d) measurements produce strong hybridization signatures under all conditions investigated, spanning phosphate buffer molarities from 0.001 to 0.5 mol L^{-1} and probe coverages from $\sim 1 \times 10^{12}$ to $\sim 7 \times 10^{12}$ cm^{-2}. The intrinsic detection sensitivity, expressed as the capacitive change per hybridization event, increased approximately 5-fold as buffer molarity decreased 50-fold from 0.5 to 0.01 mol L^{-1}. Further increase was evident in 0.001 mol L^{-1} conditions but could not be precisely quantified because the hybridized analyte coverages were too low to independently confirm.

Comparison of experimental data with theoretical calculations indicates that, at high buffer molarities, the capacitive response to hybridization can be interpreted as dominated by thinning and/or, depending on probe coverage, breakup of the MO layer as collapsed probes become converted to solvated duplexes. At low buffer molarities, the response becomes dominated by ionic effects stemming from accumulation of bound target charge. Low ionic strengths, aside from amplified diagnostic sensitivity, are attractive for other reasons. For example, by destabilizing secondary structure in nucleic acid analytes, they are expected to mitigate its biasing influence on assay results.

In general, the ability to amplify "electrostatic" detection through measurements under low ionic strengths should be possible for any uncharged nucleic acid analogue. Peptide nucleic acids (PNAs) especially have been investigated for electrochemical nucleic acid sensing. The many approaches based on PNA probes have included hybridization-mediated changes in charge transfer resistance to dissolved electroactive species such as the ferri/ferrocyanide couple,[14,36,37,42] direct oxidation of guanine bases,[39] preferential binding of electroactive indicators to the hybridized form[32,38] including electrocatalytically amplified approaches,[43] and field-effect transduction.[19,40] Low ionic strengths have been shown to dramatically improve detection in some of these methods.[42] If studies on capacitive transduction of PNA−DNA hybridization become available, they would be interesting to compare to the trends and conclusions reached for the MO probe system.

Acknowledgment. This project was supported by Award Nos. R01HG004512 and R33HG003089 from the National Human Genome Research Institute.

Supporting Information Available: Detailed description of sample preparation; summary of CV analysis for determination of strand coverages; controls for nonspecific hybridization; impact of MCP loss on the baseline in C_d measurements; derivation of the baseline function f_B. This material is available free of charge via the Internet at http://pubs.acs.org.